communications earth & environment

Article

A Nature Portfolio journal

https://doi.org/10.1038/s43247-025-02136-0

Cenozoic evolution of spring persistent rainfall in East Asia and North America driven by paleogeography

Linqiang He[1,2,3], Tianjun Zhou[1,2] ✉, Zhun Guo[4], Zikun Ren[1,2], Xiaolong Chen[1], Jie Jiang[1], Fahu Chen[5,6,7], Xu Zhang[2,5,6], Zhongyu Xiong[6], Meng Zuo[1,8], Wenmin Man[1] & Wenxia Zhang[1]

Spring persistent rainfall is a unique climate phenomenon that prevails in East Asia today, providing precious water resources to this densely populated region. However, its Cenozoic history and underlying mechanisms remain poorly understood. Here we show that the spring persistent rainfall in East Asia has emerged since the Miocene, whereas it previously flourished in North America during the Eocene, as revealed by climate models integrated with climate proxies. The contrasting evolution of spring persistent rainfall in East Asia and North America is determined by paleogeography and further influenced by CO_2-induced warming. The uplift of the Tibetan Plateau and the westward drift of the Rocky Mountains have triggered a mid-latitude Rossby wave train since the Miocene, altering the position and intensity of the subtropical highs and thus rainfall patterns. Our results illuminate the Cenozoic evolution of spring persistent rainfall, with implications for the spring climate under the extreme future warming.

Spring rains, called "as precious as oil" in ancient China, provides valuable water resources for spring revival, especially for human life and agricultural irrigation in this most densely populated region. Today, the spring persistent rainfall (SPR) is a unique synoptic and climate phenomenon in East Asia[1–3]. It brings about 600 mm of spring rainfall (March to May) to southeastern China each year, accounting for more than 35% of the total annual rainfall[4] (Supplementary Fig. 1a, b). The SPR represents the transition stage from the winter to the summer monsoon in East Asia, but it is distinct from the monsoon system itself. A weaker East Asian SPR would threaten livelihoods through consecutive droughts and frequent wildfires and delay the onset of the East Asian summer monsoon, and vice versa[5–9].

Several mechanisms have been proposed to explain the formation of the modern SPR in East Asia[10]. Initially, the zonal land–sea thermal contrast was suggested to shape the spring rainfall over southeastern China, which is due to the time lag in the seasonal warming over the western North Pacific relative to the Indochina Peninsula[1]. However, with a similar east–west thermal contrast, there is no similar heavy rain belt in North America today[2] (Supplementary Fig. 1a, b). Therefore, recent studies have proposed that the mechanical and thermal forcing of the Tibetan Plateau (TP) determines the SPR in East Asia[11–14]. Specifically, the mid-latitude westerlies deflected by the large-scale orography of the TP split into southern and northern branches, and then converge in southeastern China[2,12]. Meanwhile, the orographic gravity waves driven by the interaction between the subtropical westerlies and the small-scale orography of the TP enhance the monsoonal flow along the southern flank of the TP through the change in meridional circulation[15]. In addition, the surface heating over the TP forces a low-level cyclonic circulation around the TP through the sensible heating air pump effect[3,16]. These processes enhance the southwesterly flow, which transports the water vapor to southeastern China that forms the modern-day SPR[4].

The important roles of large-scale high orography and land-sea contrast on the East Asian SPR motivate us to understand its evolution in the geological time, which remains unknown as paleogeography has changed substantially during the Cenozoic[17]. Accordingly, we aim to investigate the Cenozoic evolution history of SPR on a global scale, especially to address when and why the present-day SPR prevails in East Asia rather than in North America. Here, we select four representative geological periods

[1]Key Laboratory of Earth System Numerical Modeling and Application, Institute of Atmospheric Physics, Chinese Academy of Sciences, Beijing, China. [2]University of Chinese Academy of Sciences, Beijing, China. [3]Lamont Doherty Earth Observatory, Columbia University, Palisades, NY, USA. [4]Climate Change Research Center, Institute of Atmospheric Physics, Chinese Academy of Sciences, Beijing, China. [5]Group of Alpine Paleoecology and Human Adaptation (ALPHA), Institute of Tibetan Plateau Research, Chinese Academy of Sciences, Beijing, China. [6]State Key Laboratory of Tibetan Plateau Earth System, Resources and Environment (TPESRE), Institute of Tibetan Plateau Research, Chinese Academy of Sciences, Beijing, China. [7]College of Earth and Environmental Sciences, Lanzhou University, Lanzhou, China. [8]State Key Laboratory of Severe Weather and Institute of Tibetan Plateau Meteorology, Chinese Academy of Meteorological Sciences, Beijing, China. ✉e-mail: zhoutj@lasg.iap.ac.cn

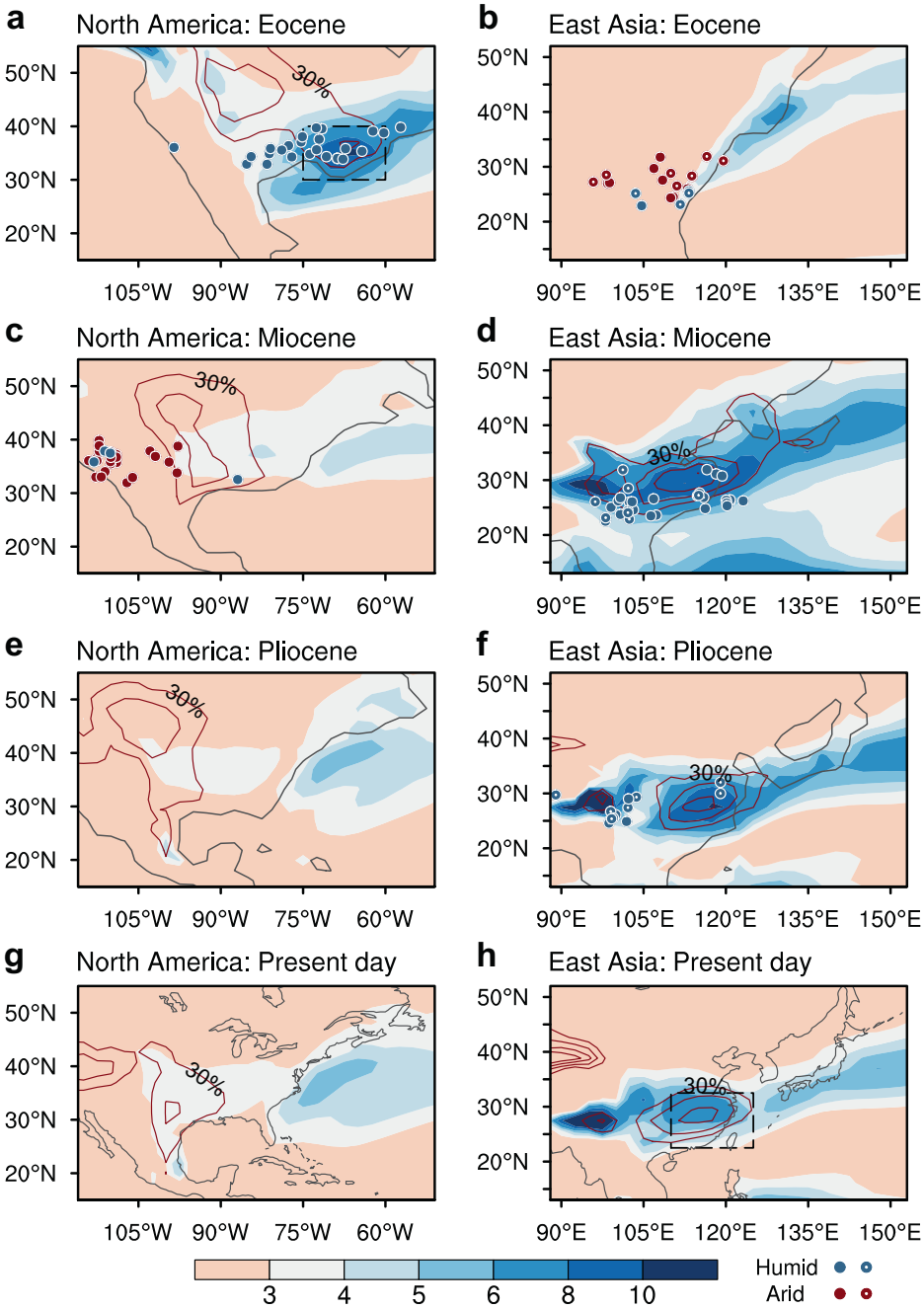

Fig. 1 | Cenozoic evolution of boreal SPR. Spring rainfall (shading, unit: mm d^{-1}) and its fraction of annual rainfall (contours, interval: 5%) over (**a**, **c**, **e**, **g**) North America and (**b**, **d**, **f**, **h**) East Asia in the Eocene, Miocene, Pliocene and present day derived from CESM coupled simulations. Filled circles, filled circles with white dots are climate proxies based on lithological and paleobotanical data, respectively, with blue (red) color representing humid (arid) climates. Dashed boxes denote the area of SPR over North America and East Asia.

during the Cenozoic, including the early Eocene (~55 million years ago (Ma), hereafter referred to simply as "Eocene")[18,19], the mid-Miocene (~15–13 Ma, hereafter referred to simply as "Miocene")[20,21], the mid-Pliocene (~3.3–3.0 Ma, hereafter referred to simply as "Pliocene")[22], and the pre-industrial period (hereafter referred to as "present day")[22]. These periods witnessed the decline of CO_2 levels (Supplementary Table 1) and important changes in global paleogeography (Supplementary Fig. 2), such as the uplift of TP and the westward drift of the Rocky Mountains. By integrating climate proxies, model simulations and physical diagnoses, we uncover the Cenozoic evolution of SPR in the northern hemisphere, which features the emergence of the East Asian SPR alongside the weakening of the North American SPR, determined by the orographic forcing.

Cenozoic evolution of SPR

To illustrate the past evolution of the boreal SPR, we first build a picture of the spring rainfall and its contribution to annual rainfall during the Eocene, Miocene, Pliocene, and present day derived from proxy records and coupled general circulation model (CGCM) simulations based on the Community Earth System Model (CESM) (see Methods; Supplementary Table 1). In the Eocene, the SPR prevailed in North America, with the spring rainfall exceeding 8 mm d^{-1} (i.e., 700 mm) and accounting for more than 35% of annual rainfall (Fig. 1a), while spring rainfall in East Asia was weak with a small percentage contribution to annual rainfall and shifted more northward along the coast compared with the present day (Fig. 1b). In the Miocene, spring rainfall in North America declined sharply, especially over land (Fig. 1c), whereas the SPR tremendously thrived in East Asia and moved southward by 10 degrees, with intensity exceeding 8 mm d^{-1} and percentage in a year exceeding 40% (Fig. 1d). The distribution of SPR in the Pliocene (Fig. 1e, f) was consistent with that in the Miocene, and persists to the present day (Fig. 1g, h).

Proxy records based on lithological and paleobotanical data agree well with the model simulations. In terms of annual mean, both indicate a humid

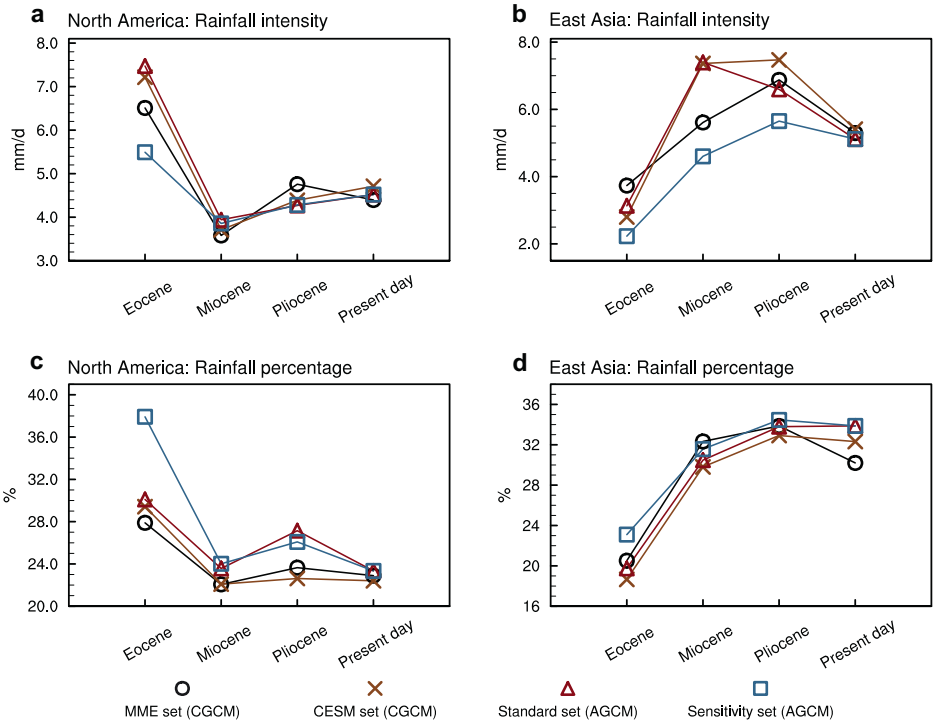

Fig. 2 | Role of paleogeography versus warming in the Cenozoic evolution of SPR. Area-averaged spring rainfall intensity (unit: mm d^{-1}) over (**a**) North America (30°–40°N, 60°–75°W) and (**b**) East Asia (22.5°–32.5°N, 110°–125°E) in the Eocene, Miocene, Pliocene and present day derived from four groups of datasets, including (1) MME set: multi-model ensemble mean or observation (i.e., Global Precipitation Climatology Project (GPCP)), (2) CESM set: coupled simulations based on CESM, (3) Standard set: CESM atmospheric simulations prescribed with the SST from the coupled simulations in four respective periods, (4) Sensitivity set: CESM atmospheric simulations prescribed with SST from the present-day coupled simulation. **c, d** As in (**a**, **b**) but for the area-averaged rainfall percentage defined as the proportion of spring rainfall to annual rainfall (%).

climate over eastern North America and an arid climate over East Asia in the Eocene, after which western North America was arid and East Asia became humid (Supplementary Fig. 1c–h). Considering the climate conditions required for proxy formation[23], the absence of widespread coal and kaolinite over eastern North America in the Miocene also suggests a drier climate compared to the Eocene, which is consistent with the coupled model simulations (Supplementary Fig. 1c, d). Meanwhile, correlations between spring rainfall evolution and the annual mean are stronger than other seasons over North America and East Asia, especially summer and autumn (Supplementary Fig. 3), suggesting that the simulated SPR evolution dominates the annual climate evolution supported by proxy records (Fig. 1). The geological evolution of SPR based on CESM simulations (see brown lines in Fig. 2) is also consistent with that derived from multi-model ensemble means (see black lines in Fig. 2). These results suggest that the SPR has emerged in East Asia but declined in North America since the Miocene.

Dominant role of changes in atmospheric circulation

To understand the physical processes responsible for the opposite evolution of SPR in North America and East Asia, we attribute the rainfall changes to the contribution of evaporation, horizontal and vertical moisture advection by diagnosing the column-integrated moisture equation[24,25] (see Methods). The results show that the decrease in spring rainfall over southeastern North America and the increase in spring rainfall over southeastern East Asia after the Eocene were mainly driven by changes in vertical moisture advection, while the effects of evaporation and horizontal moisture advection are negligible (Supplementary Fig. 4). Further decomposition of vertical moisture advection suggests that the evolution of spring rainfall was dominated by the vertical dynamic effect ($-<\omega'\partial_p\bar{q}>$) associated with vertical motion, while the vertical thermodynamic effect ($-<\bar{\omega}\partial_p q'>$) related to the Clausius–Clapeyron relationship is also evident over North America (Supplementary Fig. 5).

To illustrate the dominant role of the dynamic effect, we further analyze the associated physical fields according to the quasi-geostrophic ω equation[26,27] (see Methods). In southeastern North America, the descending anomalies (opposite sign to $-<\omega'\partial_p\bar{q}>$ in Supplementary Fig. 5b, d, f) after the Eocene can mainly be attributed to both the cold advection by anomalous northerly winds (Supplementary Fig. 6a, c, e) and negative relative vorticity advection increasing with the height by westerly winds (Supplementary Fig. 6b, d, f). In southeastern East Asia, the ascending anomalies after the Eocene mainly resulted from both the warm advection by anomalous southerly winds (Supplementary Fig. 6a, c, e) and positive relative vorticity advection increasing with the height by westerly winds (Supplementary Fig. 6b, d, f). In other words, the anomalous vertical motion in southeastern North America and southeastern East Asia was mainly related to local circulation changes (Supplementary Fig. 7a, c, e), which were part of a quasi-geostrophic Rossby wave train in the mid-latitudes (Supplementary Fig. 7b, d, f). This suggests that a circumglobal Rossby wave train in the northern hemisphere was responsible for SPR emergence in East Asia but decline in North America from the Miocene onwards.

Control of paleogeography versus CO_2-induced warming

Both paleogeography and global temperature changed substantially from the Eocene to the Miocene (Supplementary Fig. 2), which have been regarded as the main drivers of large-scale changes in atmospheric circulation[28–30]. To disentangle the roles of paleogeography and CO_2-induced warming in the quasi-geostrophic Rossby waves that dominated the past evolution of SPR, we perform two sets of numerical experiments (Supplementary Table 2). One set is the CESM standard atmospheric general circulation model (AGCM) experiments driven by the sea surface temperature (SST) predicted by the CGCM simulations in four climate periods, and the other set is the CESM sensitivity AGCM experiments prescribed with the same SST derived from the CGCM simulation in the present day.

To quantify the changes of SPR through Cenozoic, we first calculate the area-averaged spring rainfall (i.e., rainfall intensity) and its fraction of annual rainfall (i.e., rainfall percentage) over North America (30°–40°N, 60°–75°W) and East Asia (22.5°–32.5°N, 110°–125°E). The results show that the AGCM standard simulations (see red lines in Fig. 2) satisfactorily reproduced the evolution of SPR derived from the CGCM simulations (see brown lines in Fig. 2), demonstrating the feasibility of AGCM experiments to examine the source of SPR evolution. Thus, the SPR evolution in the sensitivity set (see blue lines in Fig. 2) prescribed with the present-day SST was almost driven by the paleogeography changes, and the difference of SPR

evolution between the standard set and sensitivity set was almost induced by the CO_2-induced warming.

Results show that the sensitivity set was highly consistent with the standard set in capturing the intensity and percentage of spring rainfall, suggesting the dominant role of paleogeography in controlling the evolution of SPR. Meanwhile, compared to the set of standard simulations, there existed some differences in the set of sensitivity simulations. In particular, spring rainfall was more intense in the standard set, especially over North America in the Eocene and over East Asia in the Miocene (Fig. 2a, b). This mainly resulted from the "rich-get-richer" mechanism[24,31,32], indicating the wet region/season in climatology getting wetter under the CO_2-induced warming (Supplementary Fig. 2). Meanwhile, the proportion of spring rainfall to annual rainfall was decreased in the standard set, especially over North America and East Asia in the Eocene with extreme warming (Fig. 2c, d), accompanied by an increased proportion of summer rainfall (Figure not shown). This is essentially consistent with the tropical rainfall seasonal delay under the global warming[33,34], where rainfall decreases in the onset phase and increases in the demise phase due to the increased atmospheric heat capacity and convective barriers[35–38]. In conclusion, surface warming due to the elevated CO_2 favored an increase in SPR intensity but a decrease in the rainfall percentage of SPR especially under extreme warming scenarios. These results suggest that the past evolution of SPR since Eocene was controlled by paleogeography, and further modulated by CO_2-induced warming.

Orographic forcing of the Rocky Mountains and TP

Next, we differentiate changes in paleogeography that may have caused the opposite evolution of SPR in the two regions of concern. Compared to the Eocene, there were two major mid-latitude orographic changes from the Miocene onwards—namely, westward drift of the Rocky Mountains along with the North American continent, and uplift of the TP (Supplementary Fig. 2). Accordingly, we further conduct a set of AGCM experiments prescribed with modern SST but different geography (land-sea distribution and orography) to confirm their effects (Supplementary Table 2).

To investigate the effect of westward drift of the Rocky Mountains together with the North American continent, we set the North American geography (10°–70°N, 30°–140°W) as it was in the Eocene while present-day geography is used elsewhere in the simulation (i.e., NA_cam). Results show that the North American SPR enhanced with spring rainfall exceeding 6 mm d^{-1} and accounting for more than 35% of annual rainfall, accompanied by a strengthening and northward shift of the subtropical high (Fig. 3a, c). Meanwhile, the East Asian SPR became broader and more northward-located relative to the modern pattern (Fig. 3b, d). This suggests that the westward drift of the Rocky Mountains along with the North American continent caused the decline of the North American SPR and the southward contraction of the East Asian SPR.

To examine the effect of TP uplift on the North American SPR, we prescribe the Asian topography (15°–65°N, 50°–120°E) and North American geography to its state during the Eocene and set present-day geography elsewhere in the simulation (i.e., NATP_cam). Results show that the North American SPR intensified and became closer to the SPR in the Eocene standard experiment (Fig. 3e, g). To further explore the effect of TP uplift on the East Asian SPR, we set the Asian topography alone to how it was in the Eocene and use present-day geography elsewhere in the simulation (i.e., TP_cam). Results show that the East Asian SPR vanished and was accompanied by a weakening and eastward shift of the subtropical high, consistent with that in the Eocene standard experiment (Fig. 3f, h). This indicates that the TP uplift led to the emergence of the East Asian SPR and contributed to the weakening of the North American SPR.

To clearly show the orographic forcing in the past evolution of SPR, we further examine the corresponding atmospheric circulation anomalies. Forced by the westward drift of the Rocky Mountains along with the North American continent, a quasi-barotropic Rossby wave train occurred mainly in the western hemisphere (Supplementary Fig. 8a, b); while forced by the uplift of the TP, a quasi-barotropic Rossby wave train occurred primarily in the eastern hemisphere (Supplementary Fig. 8c, d). Meanwhile, the atmospheric circulation forced by these two changes in orography was highly consistent with the difference between the present day and Eocene in the coupled simulations (Supplementary Fig. 7e, f, and Supplementary Fig. 8e, f), with a significant spatial pattern correlation coefficient of 0.78 (eddy geopotential height at 500 hPa within 10°–80°N and 0°–360°E). This suggests that the atmospheric circulation changes, which were responsible for the decline of the North American SPR and the emergence of the East Asian SPR from the Miocene onwards, were mainly driven by the westward drift of the Rocky Mountains along with the North American continent, and the uplift of the TP.

Synthesis and implications

The SPR over East Asia is now regarded as a globally unique phenomenon, but its evolution in Earth's history is poorly understood. In this study, as depicted in Fig. 4, we integrate climate proxies and model simulations to show the past evolution of the boreal SPR, revealing that the modern-day geographic distribution of the SPR has been established since the Miocene. Prior to that, SPR had prevailed in North America in the Eocene. Physical diagnoses and numerical experiments showed that the contrasting evolution of the SPR over North America and East Asia was mainly controlled by the position and intensity of the subtropical high, which was modulated by a circumglobal Rossby wave train orographically forced by the westward shift of the Rocky Mountains together with the North American continent, and the uplift of the TP. To the best of our knowledge, these results provide the first picture of the Cenozoic evolution of the SPR, and demonstrate the crucial role of orographic forcing in the decline of the North American SPR and the emergence of the East Asian SPR. Meanwhile, the surface warming induced by elevated CO_2 further affected the SPR, with an increase in spring rainfall but a decrease in its fraction of annual rainfall especially in an extreme warming environment. This suggests that, from the perspective of climate similarity[39,40], the Eocene SPR over North America could serve as a potential analog for the future spring climate over East Asia under the unmitigated emissions scenario.

Methods

Simulations of the Cenozoic SPR with CESM

As paleogeography and atmospheric CO_2 are major drivers of the past climate during the Cenozoic[28,29,39], we use four representative periods with different paleogeography and warming levels to reveal the SPR's evolution, including the Eocene (~55 Ma)[19,41], Miocene (~15–13 Ma)[21], Pliocene (~3.3–3.0 Ma)[22] and present day (pre-industrial period)[22]. These periods covered the decline in atmospheric CO_2 concentrations from 1590 ppm in the Eocene to 280 ppm in the present day, and included major paleogeography changes such as the uplift of the Tibetan Plateau the westward movement of the Rocky Mountains along with the North American continent since the Miocene. Details of the experimental designs are listed in Supplementary Table 1.

The state-of-the-art fully coupled global climate model used in our study, CESM version 1.2, was developed by the National Center for Atmospheric Research (NCAR)[42]. It includes atmosphere, land, ocean, ice, and coupler components[42]. The time-slice simulations (1.9° × 2.5°) we have performed include the Eocene, Miocene and present day[43,44], and we also integrate simulations (0.9° × 1.25°) of the Pliocene and present day derived from the NCAR[45]. In particular, the Eocene simulation is run for 2000 years because of the extremely high CO_2 concentrations[44]. The spatial pattern correlation coefficient (10°–80°N, 0°–360°E) of spring large-scale precipitation in the present day between the low- and high-resolution (regridded from 0.9° × 1.25° to 1.9° × 2.5°) simulations was 0.953 ($p < 0.001$), suggesting a negligible effect of the model resolution on our conclusion. All model data are regridded to 1.9° × 2.5°, and we averaged the last 100 years for analysis.

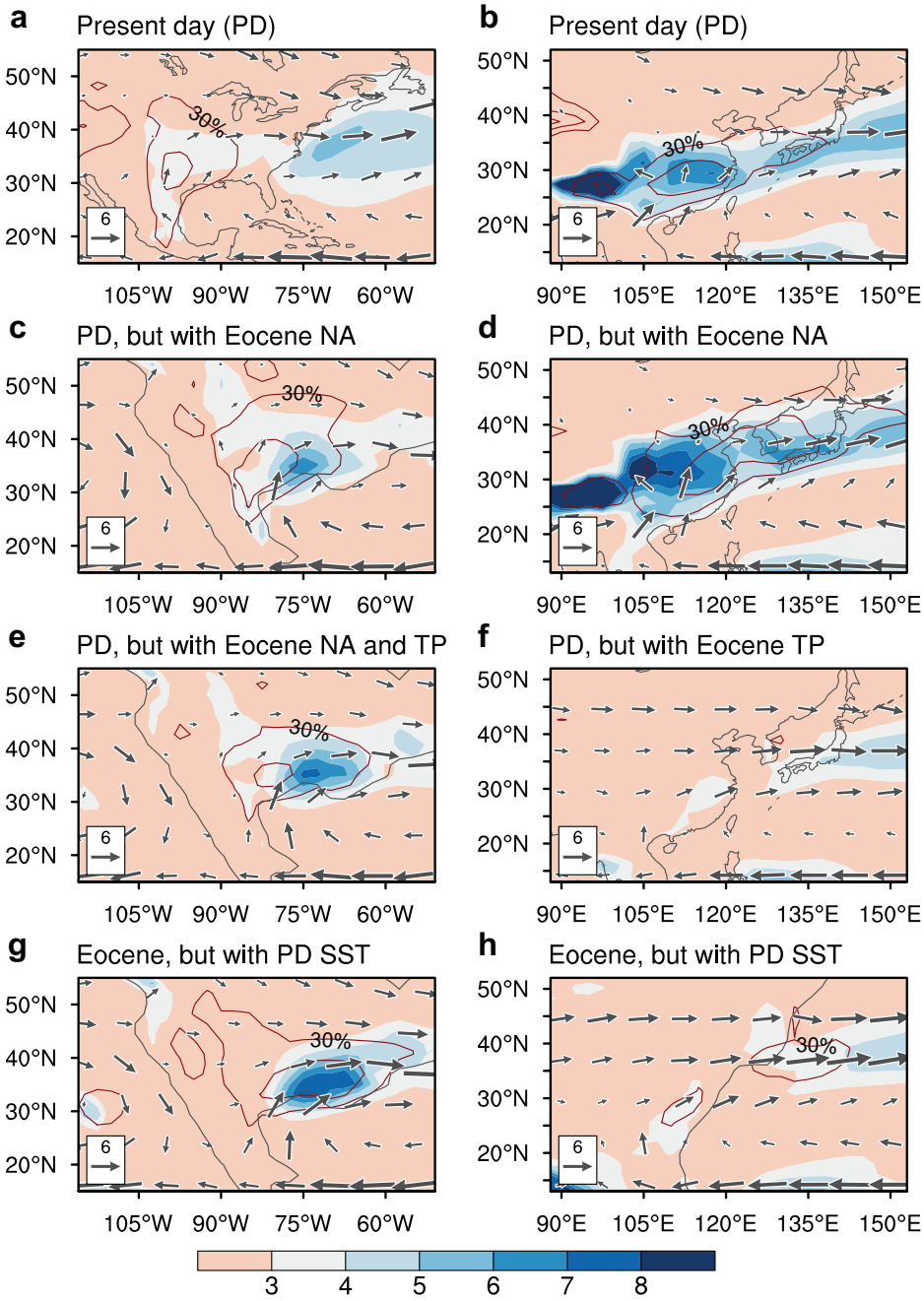

Fig. 3 | Orographic forcing of Rocky Mountains and TP. Spring rainfall intensity (shading, unit: mm d^{-1}), percentage accounting for annual rainfall (contours, interval: 10%) and horizontal wind at 850 hPa (vectors, unit: m s^{-1}) over North America (left panels) and East Asia (right panels) derived from CESM atmospheric simulations prescribed with modern-day SST but different geography (i.e., land-sea distribution and topography height). **a**, **b** modern-day geography, **c**, **d** Eocene geography over North America but present-day geography elsewhere, **e** Eocene geography over North America and Eocene topography over Asia but present-day geography elsewhere, **f** Eocene topography over Asia but present-day geography elsewhere, **g**, **h** Eocene geography.

AGCM experiments

To disentangle the effects of paleogeography and warming, we design three sets of AGCM experiments based on CESM1.2[42,46], with a resolution of 1.9° × 2.5° (Supplementary Table 2). First, we conduct a set of standard AGCM simulations for each period to reproduce the past evolution of the SPR in coupled simulations, with the prescribed SST derived from the corresponding fully coupled simulations. Second, we perform a set of AGCM sensitivity simulations for each period to separate the influence of paleogeography and warming, with the prescribed SST derived from the modern-day coupled simulation. Third, we perform a set of AGCM experiments prescribed with modern-day SST but different geography to identify the effects of the westward drift of Rocky Mountains along with the North American continent, and the TP uplift. The related forcing and boundary files are regenerated by the Paleoclimate Toolkit (PaleoToolkit) developed by NCAR when the land–sea mask is changed. All the AGCM experiments are run for 30 years, and we average the last 25 years for analysis.

Observation, proxy and multi-model synthesis

We use the global gridded precipitation from GPCP version 2.3[47], with a horizontal resolution of 2.5° from 1979 to 2019, which is an amalgamation of data from rain gauge stations, satellites, and sounding observations.

Meanwhile, we use multi-source climate proxies based on lithological and paleobotanical data, which have been synthesized in previous studies[48–50] and widely used[23,28,29,51]. Specifically, lithological proxies such as coals and kaolinites, evaporites and calcretes are commonly used as qualitative indicators of wet and dry environments in deep time, respectively[23,48]. Paleobotanical proxies, including fossils of pollen, spores and macro-plant leaves, can also reflect the climate condition[49]. For example, both palynological sediments with high proportions of fern spores, and large leaves with full margins and soft texture, indicate a humid condition, and vice versa[49]. In total, we integrate more than one hundred of proxy records based on lithological and paleobotanical data from the Eocene, Miocene, and Pliocene at the latitudes of SPR in North America and East Asia[48–50]. We rotate each

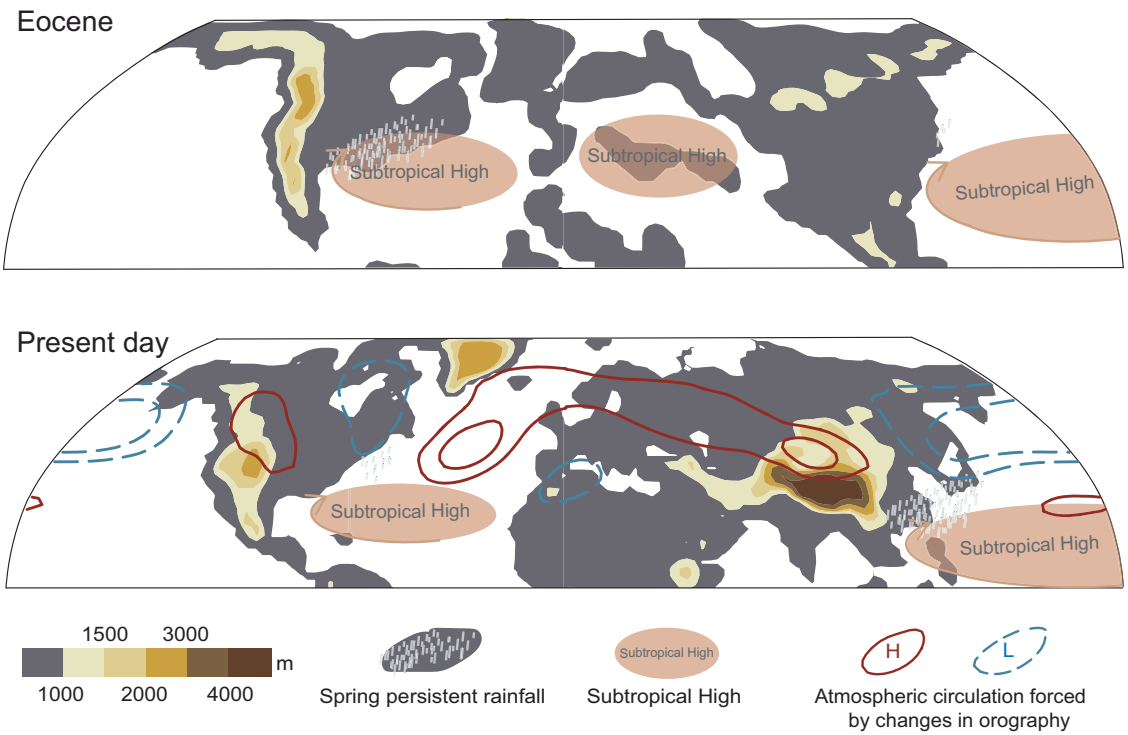

Fig. 4 | Schematic of the orographic forcing of the past evolution of SPR. The positions of the subtropical highs are derived from CESM coupled simulations, and the orographically forced atmospheric circulation changes are from the results of the atmospheric sensitivity experiments. Compared to the Eocene, the westward drift of the Rocky Mountains along with the North American continent and the uplift of the TP since the Miocene have excited a circumglobal Rossby wave train in the mid-latitudes, which has modulated the position and intensity of the subtropical highs and further led to the disappearance of the SPR in North America and its emergence in East Asia.

proxy record back to its location in the Eocene, Miocene and Pliocene using a Python tool named pyGPlates.

In addition, to reduce the effect of model uncertainty, we also analyze multi-model outputs with similar configurations including the Eocene (iCESM 1.2)[52], Miocene (FGOALS-g3)[53], and Pliocene (EC-Earth3-LR, GISS-E2-1-G, HadGEM3-GC31-LL, IPSL-CM6A-LR and NorESM1-F)[22]. In particular, we average the results of the two Eocene scenarios modeled by iCESM 1.2, as this is close to the level of global warming in this study[44,52]. Overall, our results based on CESM coupled simulations are generally consistent with the observation and multi-model ensemble mean, and are supported by the proxy records.

Moisture budget

To understand the changes in spring rainfall, we diagnose the column-integrated moisture budget[24,25], which can be described as

$$P' = E' - <\boldsymbol{V}\cdot\nabla_h q>' - <\omega\partial_p q>' + res \quad (1)$$

where primes denote the difference in boreal spring climatology (March to May) between the Miocene/Pliocene/present day and the Eocene; angular brackets represent the vertical integration from 1000 hPa to 100 hPa. P is precipitation; E is evaporation; $\boldsymbol{V}$ and ω represents the horizontal wind and vertical pressure velocity, respectively; and q is the specific humidity. The residual term res is mainly associated with transient eddies, surface boundary processes and the interpolation from the model to pressure levels[25,54]. The dominant term $-<\omega\partial_p q>'$ can be further decomposed as

$$-<\omega\partial_p q>' = -<\omega'\partial_p\bar{q}> - <\bar{\omega}\partial_p q'> - <\omega'\partial_p q'> \quad (2)$$

Here, overbars represent the spring climatology in the Eocene. The vertical dynamic component $-<\omega'\partial_p\bar{q}>$ and vertical thermodynamic component $-<\bar{\omega}\partial_p q'>$ denote the precipitation changes caused by the vertical motion (i.e., ω') and the water vapor (i.e., q'), respectively. The nonlinear component $-<\omega'\partial_p q'>$ is induced by both, which partially offsets the total contribution of the thermodynamic and dynamic components (figure not shown).

Physical mechanisms related to vertical motion

To understand the changes in vertical motion, we analyze the associated physical fields according to the quasi-geostrophic ω equation[26,27]. Neglecting the effect of atmospheric diabatic heating, the change in ω can be expressed as

$$\left(\sigma\nabla^2 + f_0^2\frac{\partial^2}{\partial p^2}\right)\omega' = f_0\frac{\partial}{\partial p}\left[\boldsymbol{V}_g\cdot\nabla\left(f+\zeta_g\right)\right]' + \frac{R}{p}\nabla^2\left(\boldsymbol{V}_g\cdot\nabla T\right)' \quad (3)$$

where $\sigma, f_0, \boldsymbol{V}_g, f, \zeta_g, R$ and T denote the static stability parameter, Coriolis parameter, geostrophic horizontal wind, planetary vorticity, geostrophic relative vorticity, dry air gas constant and air temperature, respectively. Eq 3 can be further decomposed and simplified as

$$\omega' \propto -\frac{\partial}{\partial p}\left(\bar{\boldsymbol{V}}_g\cdot\nabla\zeta_g' + \boldsymbol{V}_g'\cdot\nabla\bar{\zeta}_g + \boldsymbol{V}_g'\cdot\nabla\zeta_g' + v_g'\frac{\partial f}{\partial y}\right) \quad (4)$$
$$\text{and } \left(\bar{\boldsymbol{V}}_g\cdot\nabla T' + \boldsymbol{V}_g'\cdot\nabla\bar{T} + \boldsymbol{V}_g'\cdot\nabla T'\right)$$

Here, the physical fields associated with the dominant terms of ω changes include $-\frac{\partial}{\partial p}(\bar{\boldsymbol{V}}_g\cdot\nabla\zeta_g')$ and $\boldsymbol{V}_g'\cdot\nabla\bar{T}$. In this study, we focus on the 500 hPa pressure level, commonly regarded as part of the free atmosphere, where $\boldsymbol{V}_g$ and ζ_g are approximated by the horizontal wind $\boldsymbol{V}$ and relative vorticity ζ.

Wave activity flux

To understand the horizontal propagation of Rossby waves, we diagnose the Takaya–Nakamura wave activity flux[55], which can be expressed as

$$\begin{aligned} F_x &= \frac{1}{2|\bar{U}|}(\bar{U}(\psi'^2_x - \psi'\psi'_{xx}) + \bar{V}(\psi'_x\psi'_y - \psi'\psi'_{xy})) \\ F_y &= \frac{1}{2|\bar{V}|}(\bar{U}(\psi'_x\psi'_y - \psi'\psi'_{xy}) + \bar{V}(\psi'^2_y - \psi'\psi'_{yy})) \end{aligned} \quad (5)$$

Here, overbars denote the spring climatology in the Eocene; primes denote the difference between the Miocene/Pliocene/present day and the Eocene; U and V are the zonal and meridional wind, respectively; and $\psi = /f$ is the geopotential stream function, in which represents the geopotential.

Data availability

The GPCP dataset is available at https://climatedataguide.ucar.edu/climate-data/gpcp-monthly-global-precipitation-climatology-project. The model data we used from NCAR is available at https://www.earthsystemgrid.org/dataset/ucar.cgd.ccsm4.pliomip2.html. The main results of coupled and atmospheric simulations based on CESM are available at https://doi.org/10.5281/zenodo.14262728[56].

Code availability

The script of CESM 1.2 is available at https://www2.cesm.ucar.edu/models/cesm1.2/. The script of PyGPlates is available at https://www.gplates.org/docs/pygplates/. The script of PaleoToolkit is available at https://github.com/CESM-Development/paleoToolkit/tree/master/cesm1_2.

Received: 23 June 2024; Accepted: 14 February 2025;
Published online: 27 February 2025

References

1. Tian, S. & Yasunari, T. Climatological aspects and mechanism of spring persistent rains over Central China. *J. Meteorol. Soc. Jpn.* **76**, 57–71 (1998).
2. Wan, R. & Wu, G. Mechanism of the spring persistent rains over southeastern China. *Sci. China Ser. D. Earth Sci.* **50**, 130–144 (2006).
3. Wan, R., Zhao, B. & Wu, G. New evidences on the climatic causes of the formation of the spring persistent rains over Southeastern China. *Adv. Atmos. Sci.* **26**, 1081–1087 (2009).
4. Li, P., Zhou, T. & Chen, X. Water vapor transport for spring persistent rains over southeastern China based on five reanalysis datasets. *Clim. Dyn.* **51**, 4243–4257 (2018).
5. Zhang, L. et al. The late spring drought of 2018 in South China. *Bull. Am. Meteorol. Soc.* **93**, 1041–1067 (2020).
6. Zhou, T., Zhang, W., Zhang, L., Clark, R. & Qian, C. 2021: A year of unprecedented climate extremes in Eastern Asia, North America, and Europe. *Adv. Atmos. Sci.* **39**, 1598–1607 (2022).
7. Wang, B. & LinHo Rainy season of the Asian-Pacific summer monsson. *J. Clim.* **15**, 386–398 (2002).
8. Zhao, F. & Liu, Y. Atmospheric circulation patterns associated with wildfires in the monsoon regions of China. Geophys. Res. Lett. https://doi.org/10.1029/2019GL081932 (2019).
9. Zhu, C. W., Zhou, X. J., Zhao, P., Chen, L. X. & He, J. H. Onset of East Asian subtropical summer monsoon and rainy season in China. *Sci. China Earth Sci.* **54**, 1845–1853 (2011).
10. Chiang, J. C. H., Kong, W., Wu, C. H. & Battisti, D. S. Origins of east asian summer monsoon seasonality. *J. Clim.* **33**, 7945–7965 (2020).
11. Wu, G. et al. Tibetan Plateau climate dynamics: recent research progress and outlook. *Natl. Sci. Rev.* **2**, 100–116 (2015).
12. Wu, G. et al. The influence of mechanical and thermal forcing by the Tibetan Plateau on Asian climate. *J. Hydrometeorol.* **8**, 770–789 (2007).
13. Son, J.-H., Seo, K.-H. & Wang, B. How does the Tibetan Plateau dynamically affect downstream monsoon precipitation? *Geophys. Res. Lett.* **47**, e2020GL090543 (2020).
14. Chiang, J. C. H. et al. Role of seasonal transitions and westerly jets in East Asian paleoclimate. *Quat. Sci. Rev.* **108**, 111–129 (2015).
15. Li, R., Xu, X., Xu, X., Shepherd, T. G. & Wang, Y. Importance of orographic gravity waves over the Tibetan Plateau on the spring rainfall in East Asia. *Sci. China Earth Sci.* **66**, 2594–2602 (2023).
16. Li, J. et al. Mechanical and thermal forcings of asian large-scale orography on spring cloud amount and atmospheric radiation budget over East Asia. *J. Clim.* **36**, 5215–5232 (2023).
17. Scotese, C. R. An atlas of phanerozoic paleogeographic maps: the seas come in and the seas go out. *Annu Rev. Earth Planet Sci.* **49**, 679–728 (2021).
18. Lunt, D. J. et al. DeepMIP: model intercomparison of early Eocene climatic optimum (EECO) large-scale climate features and comparison with proxy data. *Climate* **17**, 203–227 (2021).
19. Herold, N. et al. A suite of early Eocene (~ 55 Ma) climate model boundary conditions. *Geosci. Model Dev.* **7**, 2077–2090 (2014).
20. Herold, N., Huber, M. & Müller, R. D. Modeling the miocene climatic optimum. Part I: Land and atmosphere. *J. Clim.* **24**, 6353–6373 (2011).
21. Frigola, A., Prange, M. & Schulz, M. Boundary conditions for the Middle Miocene Climate Transition (MMCT v1.0). *Geosci. Model Dev.* **11**, 1607–1626 (2018).
22. Haywood, A. M. et al. The Pliocene Model Intercomparison Project (PlioMIP) Phase 2: scientific objectives and experimental design. *Climate* **12**, 663–675 (2016).
23. Bao, X. et al. Quantifying climate conditions for the formation of coals and evaporites. *Natl. Sci. Rev.* **10**, nwad051 (2023).
24. Chou, C., Neelin, J. D., Chen, C. A. & Tu, J. Y. Evaluating the 'rich-get-richer' mechanism in tropical precipitation change under global warming. *J. Clim.* **22**, 1982–2005 (2009).
25. Seager, R., Naik, N. & Vecchi, G. A. Thermodynamic and dynamic mechanisms for large-scale changes in the hydrological cycle in response to global warming. *J. Clim.* **23**, 4651–4668 (2010).
26. Wei, W., Zhang, R., Wen, M. & Yang, S. Relationship between the Asian westerly jet stream and summer rainfall over central Asia and North China: roles of the Indian Monsoon and the South Asian high. *J. Clim.* **30**, 537–552 (2017).
27. Jiang, J. et al. Precipitation regime changes in High Mountain Asia driven by cleaner air. *Nature* **623**, 544–549 (2023).
28. Wu, F., Yang, Y. & Dupont-nivet, G. Reorganization of Asian climate in relation to Tibetan Plateau uplift. *Nat. Rev. Earth Environ.* **3**, 684–700 (2022).
29. Farnsworth, A. et al. Past East Asian monsoon evolution controlled by paleogeography, not CO2. *Sci. Adv.* **5**, eaax1697 (2019).
30. Li, T. et al. Distinctive South and East Asian monsoon circulation responses to global warming. *Sci. Bull.***67**, 762–770 (2022).
31. Chou, C. et al. Increase in the range between wet and dry season precipitation. *Nat. Geosci.* **6**, 263–267 (2013).
32. Song, F., Leung, L. R., Lu, J., Zhou, T. & Huang, P. Advances in understanding the changes of tropical rainfall annual cycle: a review. *Environ. Res. Clim.* **2**, 42001 (2023).
33. Biasutti, M. & Sobel, A. H. Delayed Sahel rainfall and global seasonal cycle in a warmer climate. *Geophys. Res. Lett.* **36**, 1–5 (2009).
34. Dwyer, J. G., Biasutti, M. & Sobel, A. H. The effect of greenhouse gas-induced changes in SST on the annual cycle of zonal mean tropical precipitation. *J. Clim.* **27**, 4544–4565 (2014).
35. Seth, A. et al. CMIP5 projected changes in the annual cycle of precipitation in monsoon regions. *J. Clim.* **26**, 7328–7351 (2013).
36. Song, F., Leung, L. R., Lu, J. & Dong, L. Seasonally dependent responses of subtropical highs and tropical rainfall to anthropogenic warming. *Nat. Clim. Chang* **8**, 787–792 (2018).

37. Song, F., Lu, J., Leung, L. R. & Liu, F. Contrasting phase changes of precipitation annual cycle between land and ocean under global warming. *Geophys. Res. Lett.* **47**, 1–14 (2020).
38. Song, F. et al. Emergence of seasonal delay of tropical rainfall during 1979–2019. *Nat. Clim. Chang* **11**, 605–612 (2021).
39. Burke, K. D. et al. Pliocene and Eocene provide best analogs for near-future climates. *Proc. Natl. Acad. Sci. USA* **115**, 13288–13293 (2018).
40. Tierney, J. E. et al. Past climates inform our future. *Science***370**, 680 (2020).
41. Kiehl, J. T., Zarzycki, C. M., Shields, C. A. & Rothstein, M. V. Simulated changes to tropical cyclones across the Paleocene-Eocene Thermal Maximum (PETM) boundary. *Palaeogeogr. Palaeoclimatol. Palaeoecol.* **572**, 110421 (2021).
42. Hurrell, J. W. et al. The community earth system model: a framework for collaborative research. *Bull. Am. Meteorol. Soc.* **94**, 1339–1360 (2013).
43. He, L. et al. Northward Extension of East Asian Summer monsoon since the Miocene set by the uplift of Tibetan plateau. *Geophys. Res. Lett.* **51**, e2023GL107262 (2024).
44. Ren, Z. et al. Enhanced "Wind-Evaporation Effect" Drove the "Deep-Tropical Contraction" in the Early Eocene. *Geophys. Res. Lett.* **51**, e2024GL108836 (2024).
45. Feng, R., Otto-Bliesner, B. L., Brady, E. C. & Rosenbloom, N. Increased climate response and earth system sensitivity from CCSM4 to CESM2 in mid-pliocene simulations. *J. Adv. Model Earth Syst.* **12**, e2019MS002033 (2020).
46. Gent, P. R. et al. The community climate system model version 4. *J. Clim.* **24**, 4973–4991 (2011).
47. Adler, R. F. et al. The version-2 global precipitation climatology project (GPCP) monthly precipitation analysis (1979-present). *J. Hydrometeorol.* **4**, 1147–1167 (2003).
48. Boucot, A. J., Xu, C., Scotese, C. R. & Morley, R. J. *Phanerozoic Paleoclimate: An Atlas of Lithologic Indicators of Climate* (Society for Sedimentary Geology, 2013).
49. Sun, X. & Wang, P. How old is the Asian monsoon system? - Palaeobotanical records from China. *Palaeogeogr. Palaeoclimatol. Palaeoecol.* **222**, 181–222 (2005).
50. Feng, R. et al. Past terrestrial hydroclimate sensitivity controlled by Earth system feedbacks. *Nat. Commun.* **13**, 1306 (2022).
51. Guo, Z. T. et al. A major reorganization of Asian climate by the early Miocene. *Climate* **4**, 153–174 (2008).
52. Tierney, J. E. et al. Spatial patterns of climate change across the Paleocene–Eocene Thermal Maximum. *Proc. Natl. Acad. Sci. USA* **119**, e2205326119 (2022).
53. Wei, J. et al. Simulation of the climate and ocean circulations in the Middle Miocene Climate Optimum by a coupled model FGOALS-g3. *Palaeogeogr. Palaeoclimatol. Palaeoecol.* **617**, 111509 (2023).
54. Chou, C., Chen, C. A., Tan, P. H. & Chen, K. T. Mechanisms for global warming impacts on precipitation frequency and intensity. *J. Clim.* **25**, 3291–3306 (2012).
55. Takaya, K. & Nakamura, H. A formulation of a phase-independent wave-activity flux for stationary and migratory quasigeostrophic eddies on a zonally varying basic flow. *J. Atmos. Sci.* **58**, 608–627 (2001).
56. He, L., Zhou, T., Guo, Z. & Ren, Z. Data for 'Cenozoic evolution of spring persistent rainfall in East Asia and North America driven by paleogeography'. [Data set]. Zenodo. https://doi.org/10.5281/zenodo.14262728 (2024).

Acknowledgements

This work is supported by the National Natural Science Foundation of China (Grant No. 41988101) and the Second Tibetan Plateau Scientific Expedition and Research (STEP) program (Grant No. 2019QZKK0102). The CESM simulations were performed at the "Earth System Numerical Simulation Facility" (EarthLab; https://cstr.cn/31134.02.EL) supported by the National Large Scientific and Technological Infrastructure project. We acknowledge the climate modeling groups that produced and provided the model simulations used in this study.

Author contributions

T.Z. conceived and designed the study, with support from L.H. L.H. conducted the analysis and drafted the manuscript. Z.G., L.H., and Z.R. performed the fully coupled climate simulations. L.H. conducted the atmospheric numerical experiments. L.H., X.Z., and Z.X. collected proxy records. T.Z., X.C., J.J., F.C., Z.X., X.Z., Z.R., M.Z., W.M., and W.Z. provided comments and revised the manuscript. All authors contributed to the scientific interpretation.

Competing interests

The authors declare no competing interests.

Additional information

Supplementary information The online version contains supplementary material available at https://doi.org/10.1038/s43247-025-02136-0.

Correspondence and requests for materials should be addressed to Tianjun Zhou.

Peer review information *Communications Earth & Environment* thanks Kana Nagashima and Swatah Borkotoky for their contribution to the peer review of this work. Primary Handling Editors: Carolina Ortiz Guerrero. A peer review file is available.